

Enhanced ultrasonic scalpel in longitudinal-bending coupled vibration based on symmetrical acoustic black hole beam structure

Cheng Chen(陈诚), Yi Wang(王怡), Huiqin Chen(陈慧琴), Chunlong Xu(徐春龙), Jianzhong Guo(郭建中), and Shuyu Lin(林书玉)

Citation: Chin. Phys. B, 2026, 35 (**7**): 074302. DOI: 10.1088/1674-1056/ae1b7a
http://cpb.iphy.ac.cn; http://iopscience.iop.org/cpb

What follows is a list of articles you may be interested in

Ultrasonic scalpel based on fusiform phononic crystal structure

Sha Wang(王莎), Junjie Shan(单俊杰), and Shuyu Lin(林书玉)
Chin. Phys. B, 2024, 33 (**10**): 104302. DOI: 10.1088/1674-1056/ad6a0c

Extension of sound field reconstruction based on element radiation superposition method in a sparsity framework

Yuan Gao(高塬), Bo-Quan Yang(杨博全), Sheng-Guo Shi(时胜国), and Hao-Yang Zhang(张昊阳)
Chin. Phys. B, 2023, 32 (**4**): 044302. DOI: 10.1088/1674-1056/ac8e55

Analysis on vibration characteristics of large-size rectangular piezoelectric composite plate based on quasi-periodic phononic crystal structure

Li-Qing Hu(胡理情), Sha Wang(王莎), and Shu-Yu Lin(林书玉)
Chin. Phys. B, 2022, 31 (**5**): 054302. DOI: 10.1088/1674-1056/ac3649

Impact vibration properties of locally resonant fluid-conveying pipes

Bing Hu(胡兵), Fu-Lei Zhu(朱付磊), Dian-Long Yu(郁殿龙), Jiang-Wei Liu(刘江伟), Zhen-Fang Zhang(张振方), Jie Zhong(钟杰), and Ji-Hong Wen(温激鸿)
Chin. Phys. B, 2020, 29 (**12**): 124301. DOI: 10.1088/1674-1056/abb312

Propagation of acoustic waves in a fluid-filled pipe with periodic elastic Helmholtz resonators

Dian-Long Yu(郁殿龙), Hui-Jie Shen(沈惠杰), Jiang-Wei Liu(刘江伟), Jian-Fei Yin(尹剑飞), Zhen-Fang Zhang(张振方), Ji-Hong Wen(温激鸿)
Chin. Phys. B, 2018, 27 (**6**): 064301. DOI: 10.1088/1674-1056/27/6/064301

Enhanced ultrasonic scalpel in longitudinal-bending coupled vibration based on symmetrical acoustic black hole beam structure

Cheng Chen(陈诚)[1,2,†], Yi Wang(王怡)[2,†], Huiqin Chen(陈慧琴)[2], Chunlong Xu(徐春龙)[1], Jianzhong Guo(郭建中)[2,‡], and Shuyu Lin(林书玉)[2,§]

[1] *School of Science, Chang'an University, Xi'an* 710064, *China*

[2] *Shaanxi Key Laboratory of Ultrasonics, Institute of Applied Acoustics, Shaanxi Normal University, Xi'an* 710119, *China*

(Received 4 September 2025; revised manuscript received 23 October 2025; accepted manuscript online 5 November 2025)

Modern minimally invasive and robotic intelligent surgeries require the miniaturization of ultrasonic scalpels (USs), resulting in a compromise in performance, which is currently an urgent technological challenge needing a breakthrough. Additionally, acoustic black holes (ABHs) have attracted widespread attention for their unique ability to capture and focus waves. Hence, a novel enhanced ultrasonic scalpel (EUS) based on symmetrical ABH beam structure in coupled vibration is proposed, capable of achieving strong, cumulative amplification of the amplitude on a short blade and effectively mitigating the performance loss caused by miniaturization. Through numerical modeling, the longitudinal and bending vibration modes of the EUS are coupled at the same frequency by adjusting the blade size. Theoretical modeling results preliminarily verify the design feasibility of the simulation and explain the physical mechanism by which the ABH effect enhances the EUS. Experimental results demonstrate that the EUS achieves a maximum vibration displacement nearly 400% greater than that of the conventional ultrasonic scalpel (CUS), along with the capability for two-dimensional cutting. This research provides theoretical and experimental references for the development of high-performance ultrasonic medical devices and explores the potential applications of ABHs in ultrasonic technology.

Keywords: ultrasonic scalpel, acoustic black hole, coupled vibration, equivalent circuit, transfer matrix

PACS: 43.40.+s, 43.35.+d, 43.38.Fx, 62.30.+d

DOI: 10.1088/1674-1056/ae1b7a **CSTR:** 32038.14.CPB.ae1b7a

1. Introduction

Ultrasonic scalpels (USs), with the advantages of fast cutting, high flexibility, less bleeding, no smoke production, and minimal side effects, have gradually become the preferred energy-type instruments in almost all surgical fields.[1–5] However, with the advancement of modern surgical procedures, there are more diverse performance requirements for the USs, such as miniaturization, increased cutting dimensions, greater amplitude, enhanced acoustic energy radiation, and advanced materials.[6] Among these requirements, the demand for miniaturization is mainly driven by minimally invasive and robotic intelligent surgeries.[7] The conventional US design, which is based on a slender rod structure, presents several drawbacks, including challenges in controlling vibrations, limited operational flexibility, high cost, and potential for physician fatigue. However, due to the limited power capacity of piezoelectric ceramics and the reduction in gain structures, the miniaturization of the USs may result in a decrease in cutting efficiency. Therefore, finding ways to enhance the performance of miniaturized USs has become an urgent technical challenge requiring breakthroughs.

To address this issue, Li *et al.*[8] conducted an in-depth exploration of the opportunities and limitations of miniaturizing the USs based on Langevin transducers, providing important insights into the trade-off between size, piezoelectric ceramic material volume, resonance frequency, and achievable vibration amplitude. Chen *et al.*[9] developed a high-performance ultrasonic scalpel transducer using the relaxor-based ferroelectric single crystal PIMNT, which significantly enhanced power output performance while reducing the transducer's size. In addition to systematic research on transducers, numerous studies have shown that combining multiple vibration modes can improve the performance of ultrasonic surgical instruments, such as longitudinal–torsional coupling and longitudinal–bending coupling.[10–13] Prominently, Yao *et al.*[14] proposed an ultrasonic elliptical vibration-assisted electrosurgical cutting system for cold cutting and preventing tissue accumulation, and achieved the longitudinal-bending mode coupling at the same frequency by changing the size of the blade. From a practical and economic perspective, adjusting the blade's size to realize multimodal coupling can be a simpler and more efficient approach, potentially offering an optimal solution for improving the vibration performance of the USs.

Furthermore, acoustic black holes (ABHs), as novel func-

[†]These authors contributed equally to this work.

[‡]Corresponding author. E-mail: guojz@snnu.edu.cn

[§]Corresponding author. E-mail: sylin@snnu.edu.cn

© 2026 Chinese Physical Society and IOP Publishing Ltd. All rights, including for text and data mining, AI training, and similar technologies, are reserved.

tional structures for sound wave capturing and focusing, have been widely applied in various acoustic fields.[15,16] Currently, ABHs are primarily categorized into two types: sound black holes (SBHs) and vibration black holes (VBHs). The fundamental design principle of SBHs involves tailoring the inner diameter of a pipe to vary axially according to a power-law profile, combined with the use of Helmholtz resonators[17,18] or other sound-absorbing materials,[19] to achieve efficient sound wave absorption. VBHs, on the other hand, incorporate a power-law profile into the geometry of elastic structures (such as beams,[20] plates,[21] rings,[22] or helices[23]). This causes the speed of propagating flexural waves to gradually decrease and their amplitude to continuously amplify, thereby localizing vibrational energy at the structural tip. By adding damping materials to the tip region, efficient vibration suppression can be achieved.[24,25] Additionally, VBHs have demonstrated significant potential for application in various fields, including energy harvesting,[26] wave control,[27] and particle manipulation.[28–30]

Leveraging the unique sound wave focusing and energy localization characteristics of ABHs, we have previously successfully applied them to the long-shaft ultrasonic scalpel[31] and immersed sonoreactor.[32] The results indicate that the incorporation of ABHs significantly enhances the cutting and hemostatic performance of long-shaft ultrasonic scalpels, while also expanding the scope and intensity of acoustic cavitation in the immersed sonoreactor.

In this paper, we aim to further explore the potential of ABHs in enhancing the performance of miniaturized ultrasonic devices. It is worth noting that the thin-walled profile of acoustic black holes is naturally compatible with miniaturized ultrasonic devices. Based on this, this paper proposes a novel enhanced ultrasonic scalpel (EUS) with a symmetrical ABH blade in coupled vibration, aiming to resolve the performance loss problem caused by miniaturization. The main work is as follows. In Section 2, the initial design dimensions of the EUS in coupled vibration are obtained through numerical modeling. Section 3 conducts a theoretical analysis to investigate the potential physical mechanisms of the EUS. Section 4 further compares the performance of the EUS and the CUS using the FEM, discussing the improvements resulting from structural upgrades. In Section 5, the EUS and the CUS prototypes are fabricated and experimentally validated.

2. Numerical modeling

Figure 1 shows the EUS and its sectional diagram, which consists of an ultrasonic transducer, a concentrator, and an ABH blade. The piezoelectric transducer is composed of a back cover plate, a piezoelectric ceramic stack, and a front cover plate. Among them, R_1, R_2, L_1, L_2 are the radii and lengths of the two circular section rods of the back cover plate, R_0, R_2, L_0 are the inner and outer radii and thickness of a single piezoelectric ceramic ring, with the number of rings being 4, R_2, R_3 are the radii of the big end and small end of the circular front cover plate, L_3, L_4, L_5 are the lengths of the big end circular rod, the conical variable section rod and the small end circular rod of the front cover plate. The concentrator is a composite ultrasonic transformer with a conical transition section. R_5, L_6 are the radius and length of the big end circular rod of the concentrator, R_6, L_7 are the radius and length of the flange, L_8 is the length of the conical transition section of the concentrator, R_7, L_9 are the radius and length of the small end circular rod of the concentrator. The concentrator and ABH blade are connected by a bolt, R_9 and L_{11} are the radius and length of the bolt. The ABH blade consists of a circular rod with a uniform cross-section and a rectangular rod with variable cross-section. R_8 and L_{10} represent the radius and length of the circular rod, H_0 is the half truncation height of the rectangular rod, H_1 is the half maximum height of the rectangular rod, and L_{ABH} is the length of the rectangular rod. The cross-section height function of the rectangular rod is

$$H(x) = \frac{H_1 - H_0}{L_{\mathrm{ABH}}^m} x^m + H_0, \tag{1}$$

where m is the height change coefficient ($m \geq 2$).

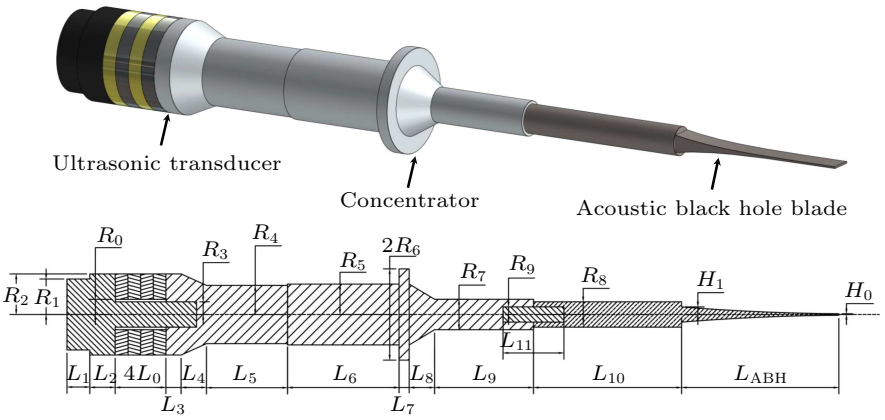


Fig. 1. The EUS and its sectional diagram.

Table 1. Material and geometrical parameters of the EUS.

Parameters	Value	Parameters	Value	Parameters	Value
ρ_1 (kg/m^3)	7850	σ_3	0.3	L_0 (mm)	2.5
E_1 (N/m^2)	2.05×10^{11}	R_0 (mm)	3	L_1 (mm)	4.5
σ_1	0.28	R_1 (mm)	7	L_2 (mm)	5
ρ_0 (kg/m^3)	7600	R_2 (mm)	8	L_3 (mm)	3
s_{33}^{D} (m^2/N)	13.5×10^{-10}	R_3 (mm)	2.5	L_4 (mm)	5
d_{31} (C/N)	-9.7×10^{-11}	R_4 (mm)	5.75	L_5 (mm)	16
d_{33} (C/N)	2.25×10^{-10}	R_5 (mm)	6	L_6 (mm)	19.8
$\varepsilon_{33}^{\mathrm{T}}$ (Cm^{-1})	8.842×10^{-9}	R_6 (mm)	9	L_7 (mm)	2
k_{33}	0.64	R_7 (mm)	3	L_8 (mm)	5
ρ_2 (kg/m^3)	2700	R_8 (mm)	2.5	L_9 (mm)	17.7
E_2 (N/m^2)	7×10^{10}	R_9 (mm)	1.5	L_{10} (mm)	29.2
σ_2	0.33	H_0 (mm)	0.15	L_{11} (mm)	12
ρ_3 (kg/m^3)	4500	H_1 (mm)	1.5	L_{ABH} (mm)	31
E_3 (N/m^2)	1.10×10^{11}	m	4.19515	P	4

Based on the solid mechanics module and the static electricity module of the commercial software COMSOL Multiphysics, the numerical modeling of the EUS is established using the finite element method (FEM). The transducer, concentrator, and ABH blade are simultaneously designed as three longitudinal vibration half-wave oscillators, and their axial dimensions are preliminarily determined. Then, by continuously adjusting the size of the blade (mainly the truncation height $2H_0$ and height change coefficient m), the high-order bending vibration frequency of the EUS is tuned to approach its third-order longitudinal vibration frequency infinitely closely.

In the FEM, the elastic boundary of the EUS is mechanically free and the applied voltage is 1 V. By establishing a rotating coordinate system, the polarization directions of two piezoelectric ceramic rings are along the $-z$ axis (while the other two rings are along the $+z$ axis). The material of the back cover plate and the bolt is steel, the piezoelectric stack material is PZT-8, the material of the front cover plate and concentrator is aluminum, and the material of the ABH blade is titanium alloy. The specific material parameters of the EUS are shown in Table 1. The effects of external loads and losses are ignored. The final design dimensions obtained are shown in Table 1. Additionally, given that the blade tip is extremely thin, an ultra-fine mesh was used during the meshing process to ensure the accuracy of the simulation calculations.

Figure 2(a) illustrates the mode of the EUS with third-order longitudinal vibration coupled with high-order bending vibration at a frequency of 55490 Hz. Figure 2(b) shows the high-order bending vibration mode of the EUS at a frequency of 55493 Hz. It can be observed that bending vibration mode coupling mainly occurs at the variable-cross-section short blade, which can be approximated as the seventh-order bending vibration mode of a fixed-free rod. The transducer and concentrator barely undergo bending deformation, which is beneficial for reducing sound energy loss during transmission.

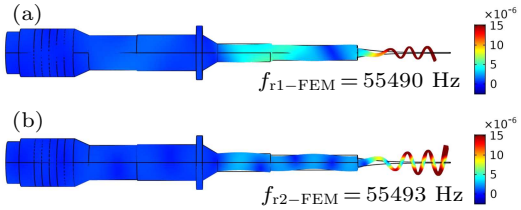


Fig. 2. (a) The longitudinal-bending coupled vibration mode of the EUS at a frequency of 55490 Hz. (b) The high-order bending vibration mode of the EUS at a frequency of 55493 Hz.

3. Theoretical analysis

3.1. Electromechanical equivalent circuit of the EUS in longitudinal vibration

To more accurately grasp the design principles and physical mechanism, we conducted theoretical modeling analysis on the EUS. Firstly, the electromechanical equivalent circuit model (EECM) is employed to analyze the longitudinal vibration of the EUS. Due to the complex variation in the cross-sectional height of the rectangular rod, it is challenging to model the EUS using general vibration theory. Therefore, we utilize the step-reduction method to theoretically model the variable cross-section rectangular rod.[33] The variable cross-section rectangular rod is divided into N rectangular rods with uniform cross-sections and mechanically interconnected along the axis. The transfer matrix model (TMM) of longitudinal vibration of the i-th uniform cross-section rod can be expressed as

$$\begin{bmatrix} v_{i1} \\ F_{i1} \end{bmatrix} = \begin{bmatrix} a_{11}^i & a_{12}^i \\ a_{21}^i & a_{22}^i \end{bmatrix} \begin{bmatrix} v_{i2} \\ F_{i2} \end{bmatrix} = \begin{bmatrix} \cos\left(\frac{\omega L_i}{c_0}\right) & \frac{\mathrm{j}}{\rho_3 c_3 h_i b_i} \sin\left(\frac{\omega L_i}{c_0}\right) \\ \mathrm{j}\rho_3 c_3 h_i b_i \sin\left(\frac{\omega L_i}{c_0}\right) & \cos\left(\frac{\omega L_i}{c_0}\right) \end{bmatrix} \begin{bmatrix} v_{i2} \\ F_{i2} \end{bmatrix} = [M_{i\mathrm{L}}] \begin{bmatrix} v_{i2} \\ F_{i2} \end{bmatrix}, \tag{2}$$

where $v_{i1/2}$ is the longitudinal vibration velocity, $F_{i1/2}$ is the longitudinal force, $i = 1, 2, 3, \ldots, N$, and a^i_{11}, a^i_{12}, a^i_{21}, a^i_{22} are the longitudinal vibration influencing factors of the i-th uniform cross-section rod. Then, the longitudinal vibration TMM of the variable cross-section rectangular rod can be expressed as

$$[M_{\mathrm{L}}] = \prod_{i=1}^{N} [M_{i\mathrm{L}}] = \begin{bmatrix} A_{11} & A_{12} \\ A_{21} & A_{22} \end{bmatrix}, \tag{3}$$

where A_{11}, A_{12}, A_{21}, A_{22} are the longitudinal vibration influencing factors of the variable cross-section rectangular rod. According to Eq. (3), the expressions for the force and velocity of the longitudinal vibration of the variable cross-section rectangular rod can be written as

$$F_{\mathrm{L1}} = (Z_{24} + Z_{25})v_{\mathrm{L1}} + Z_{25}v_{\mathrm{L2}} + U, \tag{4}$$

$$F_{\mathrm{L2}} = (Z_{23} + Z_{25})\, v_{\mathrm{L2}} + Z_{25}v_{\mathrm{L1}}, \tag{5}$$

where Z_{23}, Z_{24}, Z_{25} are the equivalent mechanical impedances of the variable cross-section rectangular rod; v_{L1} and v_{L2} are the equivalent vibration velocities; U is the current controlled voltage source, used as a circuit compensation element for structural asymmetry.[34] Using the continuity conditions of force and vibration velocity between constituent components, the electromechanical equivalent circuit of the EUS in longitudinal vibration is obtained, as shown in Fig. 3. The specific expressions for each element of the EUS are shown in the Appendix.[35]

Then simplify the circuit:

$$Z_{\mathrm{M12}} = Z_{23} + Z_{25} - \frac{Z_{25}}{Z_{23} + Z_{24}}\left(Z_{25} + \frac{U}{v_{\mathrm{L2}}}\right), \tag{6}$$

$$Z_{\mathrm{M11}} = Z_{21-2} + \frac{(Z_{21-2} + Z_{\mathrm{M12}})Z_{22-2}}{Z_{21-2} + Z_{22-2} + Z_{\mathrm{M12}}}, \tag{7}$$

$$Z_{\mathrm{M10}} = Z_{21-1} + Z_{01-2} + \frac{(Z_{21-1} + Z_{01-2} + Z_{\mathrm{M11}})(Z_{22-1} + Z_{02-2})}{Z_{21-1} + Z_{01-2} + Z_{\mathrm{M11}} + Z_{22-1} + Z_{02-2}}, \tag{8}$$

$$Z_{\mathrm{M9}} = Z_{19-2} + Z_{01-1} + \frac{(Z_{19-2} + Z_{01-1} + Z_{\mathrm{M8}})(Z_{20-2} + Z_{02-1})}{Z_{19-2} + Z_{01-1} + Z_{\mathrm{M8}} + Z_{20-2} + Z_{02-1}}, \tag{9}$$

$$Z_{\mathrm{M8}} = Z_{19-1} + \frac{(Z_{19-1} + Z_{\mathrm{M7}})Z_{20-1}}{Z_{19-1} + Z_{\mathrm{M7}} + Z_{20-1}}, \tag{10}$$

$$Z_{\mathrm{M7}} = Z_{16} + \frac{(Z_{17} + Z_{\mathrm{M8}})Z_{18}}{Z_{17} + Z_{18} + Z_{\mathrm{M8}}}, \tag{11}$$

$$Z_{\mathrm{M6}} = Z_{14} + \frac{(Z_{14} + Z_{\mathrm{M7}})Z_{15}}{Z_{14} + Z_{15} + Z_{\mathrm{M7}}}, \tag{12}$$

$$Z_{\mathrm{M5}} = Z_{12} + \frac{(Z_{12} + Z_{\mathrm{M6}})Z_{13}}{Z_{12} + Z_{13} + Z_{\mathrm{M6}}}, \tag{13}$$

$$Z_{\mathrm{M4}} = Z_{10} + \frac{(Z_{10} + Z_{\mathrm{M5}})Z_{11}}{Z_{10} + Z_{11} + Z_{\mathrm{M5}}}, \tag{14}$$

$$Z_{\mathrm{M3}} = Z_{7} + \frac{(Z_{8} + Z_{\mathrm{M4}})Z_{9}}{Z_{8} + Z_{9} + Z_{\mathrm{M4}}}, \tag{15}$$

$$Z_{\mathrm{M2}} = Z_{5} + \frac{(Z_{5} + Z_{\mathrm{M3}})Z_{6}}{Z_{5} + Z_{6} + Z_{\mathrm{M3}}}, \tag{16}$$

$$Z_{\mathrm{M1}} = Z_{3} + \frac{(Z_{3} + Z_{\mathrm{M0}})Z_{4}}{Z_{3} + Z_{4} + Z_{\mathrm{M0}}}, \tag{17}$$

$$Z_{\mathrm{M0}} = Z_{1} + \frac{Z_1 Z_2}{Z_1 + Z_2}. \tag{18}$$

The equivalent mechanical impedance Z_{m} of the EUS can be expressed as

$$Z_{\mathrm{m}} = Z_{\mathrm{p2}} + \frac{(Z_{\mathrm{p1}} + Z_{\mathrm{M1}})(Z_{\mathrm{p1}} + Z_{\mathrm{M2}})}{Z_{\mathrm{p1}} + Z_{\mathrm{M1}} + Z_{\mathrm{p1}} + Z_{\mathrm{M2}}}. \tag{19}$$

The input electric impedance Z_{e} of the EUS is

$$Z_{\mathrm{e}} = \frac{Z_{\mathrm{m}}}{n_2 + \mathrm{j}\omega P C_0 Z_{\mathrm{m}}}. \tag{20}$$

From Eq. (20), the resonance frequency equation is

$$Z_{\mathrm{e}} = 0. \tag{21}$$

Meanwhile, the anti-resonance frequency equation is

$$1/Z_{\mathrm{e}} = 0. \tag{22}$$

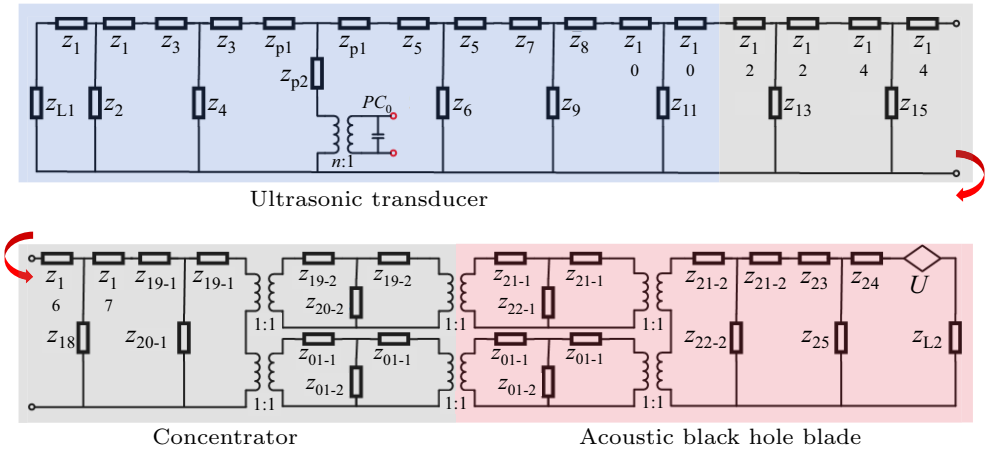


Fig. 3. The electromechanical equivalent circuit of the EUS in longitudinal vibration.

Since the resonance frequency equation of the EUS is a transcendental equation, MATLAB R2018b is used to solve it. Figure 4 shows the electrical impedance frequency response curves of the EUS obtained by the EECM and the FEM. The calculated resonance frequency $f_{\mathrm{r-EECM}}$ and anti-resonance frequency $f_{\mathrm{a-EECM}}$ of the EUS by the EECM are 55041 Hz and 55245 Hz, slightly lower than the frequencies calculated by the FEM ($f_{\mathrm{r1-FEM}} = 55490$ Hz, $f_{\mathrm{a1-FEM}} = 55619$ Hz), with the errors of 0.8% and 0.6%. The errors come from the established EECM, which is based on 1D longitudinal vibration theory and ignores coupling effects of the non-design vibration mode.

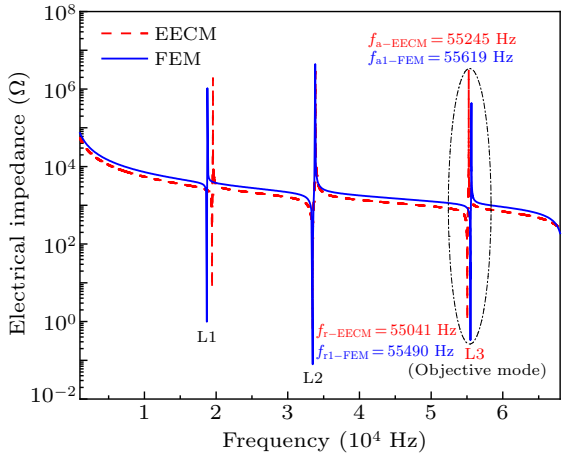


Fig. 4. The electrical impedance frequency response curves of the EUS obtained by the EECM and the FEM.

3.2. Transfer matrix of ABH blade in bending vibration

The variable cross-section rectangular rod of the ABH blade is approximated as a fixed-free bending vibration rod to analyze the local bending vibration. By continuing to use the step-reduction method, the bending vibration transfer matrix of the i-th uniform cross-section rod can be expressed as[33,36]

$$\begin{bmatrix} w_{i1} \\ \varphi_{i1} \\ M_{i1} \\ Q_{i1} \end{bmatrix} = \begin{bmatrix} b^i_{11} & b^i_{12} & b^i_{13} & b^i_{14} \\ b^i_{21} & b^i_{22} & b^i_{23} & b^i_{24} \\ b^i_{31} & b^i_{32} & b^i_{33} & b^i_{34} \\ b^i_{41} & b^i_{42} & b^i_{43} & b^i_{44} \end{bmatrix} \begin{bmatrix} w_{i2} \\ \varphi_{i2} \\ M_{i2} \\ Q_{i2} \end{bmatrix} = [M_{i\mathrm{B}}] \begin{bmatrix} w_{i2} \\ \varphi_{i2} \\ M_{i2} \\ Q_{i2} \end{bmatrix}, \quad (23)$$

where $1 \le i \le N$, $w_{i1/2}$ is the lateral displacement, $\varphi_{i1/2}$ is the torsion angle, $M_{i1/2}$ is the bending moment, $Q_{i1/2}$ is the shear force, b^i_{11}, b^i_{12}, b^i_{13}, b^i_{14}, b^i_{21}, b^i_{22}, b^i_{23}, b^i_{24}, b^i_{31}, b^i_{32}, b^i_{33}, b^i_{34}, b^i_{41}, b^i_{42}, b^i_{43}, b^i_{44} are the bending vibration influencing factors of the i-th uniform cross-section rod, and the detailed expressions of them can be found in Refs. [31,36]. Then, the bending coupled vibration transfer matrix of the variable cross-section rectangular rod can be expressed as

$$[M_{\mathrm{B}}] = \prod_{i=1}^{N} [M_{i\mathrm{B}}] = \begin{bmatrix} B_{11} & B_{21} & B_{31} & B_{41} \\ B_{21} & B_{22} & B_{23} & B_{24} \\ B_{31} & B_{32} & B_{33} & B_{34} \\ B_{41} & B_{42} & B_{43} & B_{44} \end{bmatrix}, \quad (24)$$

where $B_{11}, B_{12}, B_{13}, B_{14}, B_{21}, B_{22}, B_{23}, B_{24}, B_{31}, B_{32}, B_{33}, B_{34}, B_{41}, B_{42}, B_{43}, B_{44}$ are the bending vibration influencing factors of the variable cross-section rectangular rod. According to Eq. (24), the bending vibration frequency equation for the variable cross-section rectangular rod under fixed-free boundary conditions can be obtained as follows:

$$B_{33}B_{34} - B_{43}B_{44} = 0. \quad (25)$$

The number of divisions, N, of the blade is set to 100 to ensure calculation accuracy. Figure 5 shows the characteristic solution curve of the bending vibration frequency equation of the variable cross-section rectangular rod under fixed-free boundary conditions. In the frequency range of 0–70000 Hz, there are seven roots of Eq. (25), corresponding to seven orders of bending vibration frequencies. The seventh-order frequency value is 54398 Hz, with an error of only 2% compared to the FEM results ($f_{\mathrm{r1-FEM}} = 55493$ Hz), which can provide theoretical support for numerical modeling analysis and verify the feasibility of adjusting the size to achieve modal coupling.

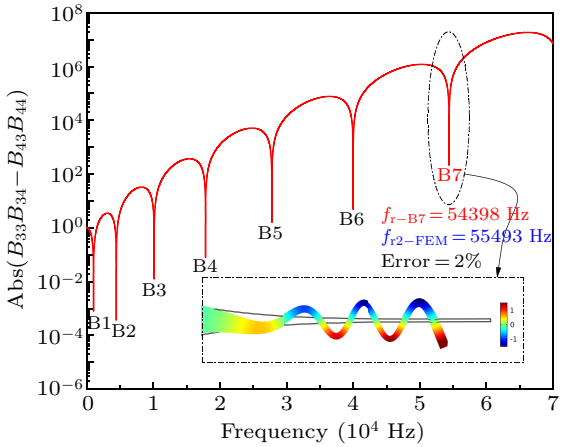


Fig. 5. The characteristic solution curve of the bending vibration frequency equation of the variable cross-section rectangular rod under fixed-free boundary conditions.

3.3. Enhancement mechanism of the ABH effect

The underlying mechanism of the ABH effect on enhancing the EUS is explored theoretically. Considering the bending wave propagation in the ABH blade, the local wave number, wave velocity, and amplitude can be expressed as[16]

$$k(x) = \left[\frac{12\rho_3(1-\sigma_3^2)\omega^2}{E_3 H(x)^2}\right]^{1/4}, \quad (26)$$

$$c(x) = \frac{\omega}{k} = \sqrt{\omega H(x)}\left[\frac{E_3}{12\rho_3(1-\sigma_3^2)}\right]^{1/4}, \quad (27)$$

$$A(x) = A_0\left[\frac{H_1}{H(x)}\right]^{3/4}. \quad (28)$$

Here, ρ_3 is the density, σ_3 is Poisson's ratio, ω is the angular frequency, and E_3 is Young's modulus. In an ideal scenario, as the truncation height H_0 approaches zero, the bending wave number $k(0)$ tends to infinity and velocity $c(0)$ tends to zero. This implies that the bending wave cannot reach the tip of

the ABH blade, and the tip can be considered a singularity where the energy density and amplitude $A(0)$ approach infinity. However, in practical applications, achieving zero truncation height is impossible. Nevertheless, even with non-zero truncation heights, the EUS can still achieve a longer amplitude amplification time as the wave velocity decreases. This ability to significantly amplify the amplitude in a short blade length can be an effective solution to address the limited vibration capacity caused by miniaturization.

4. Performance comparison

In this section, we numerically investigate the performance enhancement of the EUS by embedding an ABH profile, in comparison with the CUS of the same length. Unlike the EUS with a power-law varying ABH blade ($m = 4.195$), the CUS has a linearly varying rectangular cross-section blade ($m = 1$). In the FEM, the mechanical boundary conditions for both USs are free, and the excitation voltage is 1 V.

Figure 6 shows the blade surface vibration displacement distribution of two USs obtained by the FEM. It can be observed that the axial displacement of the CUS blade exhibits a gradually increasing trend near the cutting head, while there is almost no significant lateral displacement. This indicates that the CUS can only perform one-dimensional (1D) cutting work in a simple axial extension mode. However, besides progressive axial displacement, the EUS demonstrates considerable lateral bending displacement, allowing it to employ a more efficient coupled motion of axial extension and lateral bending for two-dimensional cutting. This enables more precise and efficient tissue separation and dissection during surgery. Such a capability not only improves cutting accuracy and controllability while minimizing damage to adjacent healthy tissues, but also streamlines surgical maneuvers by enabling multi-directional motion through a single incision, thereby reducing operative time.

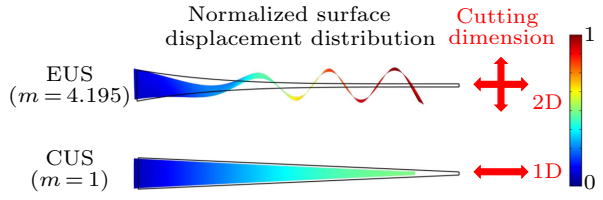


Fig. 6. The blade surface displacement distribution and cutting dimensions of the EUS and the CUS obtained by the FEM.

Subsequently, we extracted and normalized the vibration displacements of two USs for better performance comparison, as shown in Fig. 7. It can be observed that, compared with the CUS, after embedding the ABH features, the maximum total vibration displacement amplitude of the EUS increased by nearly 10 times (Fig. 7(a)). Furthermore, Fig. 7(b) illustrates the lateral displacements of the two USs. In the ABH blade, the bending wave number increases significantly, and the amplitude of bending vibration amplifies cumulatively and strongly, which is consistent with the results of the theoretical analysis and verifies the feasibility of structural upgrading. It should be emphasized that, unlike conventional amplitude amplifiers, the ABH structure offers a significant advantage in stronger amplitude amplification over the same distance range due to the reduction in wave speed, which is crucial for addressing the problem caused by miniaturization.

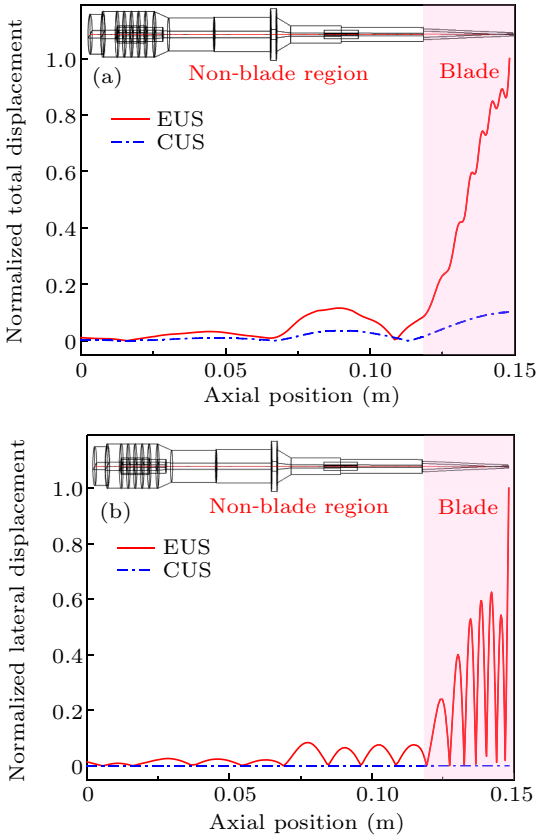


Fig. 7. The normalized displacement comparison of the EUS and the CUS obtained by the FEM, (a) total, (b) lateral.

5. Experiment verification

To further validate the aforementioned analysis, prototypes of both the EUS and CUS are fabricated, as depicted in Fig. 8. Both prototypes utilize a shared transducer and concentrator to minimize errors in performance comparison. The transducer consists of a steel back cover plate, four PZT-8 rings, and an aluminum front cover plate, with Cu electrodes incorporated within the piezoelectric stack for electrical excitation application. The concentrator is manufactured from aluminum and integrated with the aluminum front cover plate. A steel bolt is used to connect the concentrator and the blade. The specific geometrical dimensions are presented in Table 1. The impedance analysis experiment and vibration testing comparative experiment are conducted to verify the actual operability of the EUS and explore the impact of embedding the ABH structure on the performance improvement.

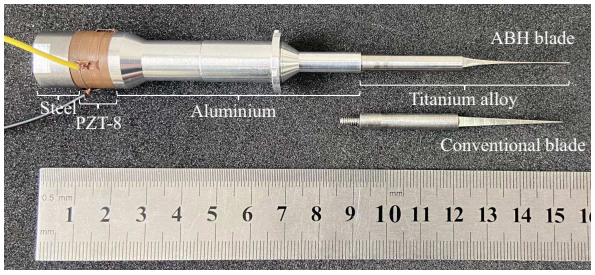


Fig. 8. The EUS prototype and the CUS blade.

The electrical impedance frequency response of the EUS is measured using the WK6500B precision impedance analyzer, as shown in Fig. 9(a). The frequency scanning range is set from 53 kHz to 60 kHz, with an excitation voltage amplitude of 1 V. The obtained frequency response curves of the electrical impedance and phase are shown in Fig. 9(b). Within the measurement frequency range, two impedance valleys can be observed, corresponding to the longitudinal-bending coupled vibration and high-order bending vibration of the EUS. The measured resonance frequencies corresponding to the two modes are 56278 Hz and 56511 Hz, with errors of 1.4% and 1.8% compared to the frequency values obtained by the FEM (55490 Hz and 55493 Hz). The reasons for the errors include: 1) The use of standard material parameters in the FEM differs from those of the actually manufactured EUS, especially titanium alloys. 2) The mechanical/dielectric loss and load of the EUS are neglected in the FEM, which cannot be disregarded in experimental measurements. 3) The pre-stress is applied to the transducer during the actual processing to ensure structural strength, which impacts the frequency due to the difficulty in accurate control.

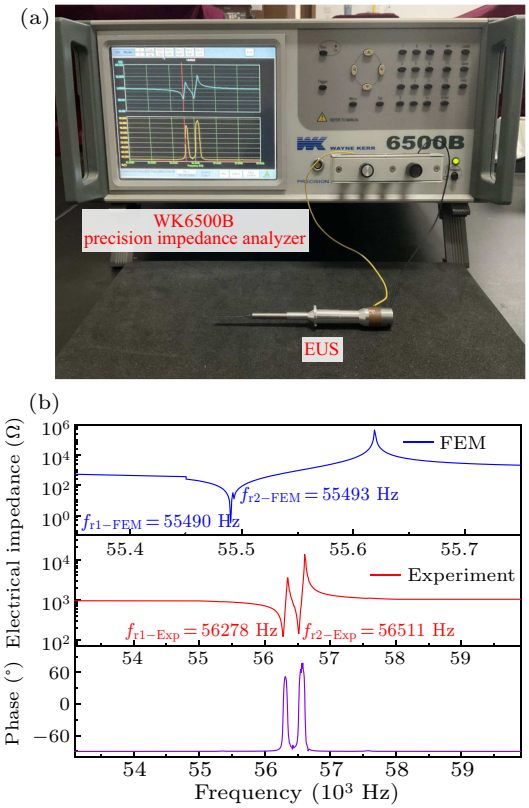


Fig. 9. (a) The impedance analysis experiment of the EUS by using WK6500B precision impedance analyzer. (b) The frequency response curves of electrical impedance (FEM & Experiment) and vibration phase of the EUS.

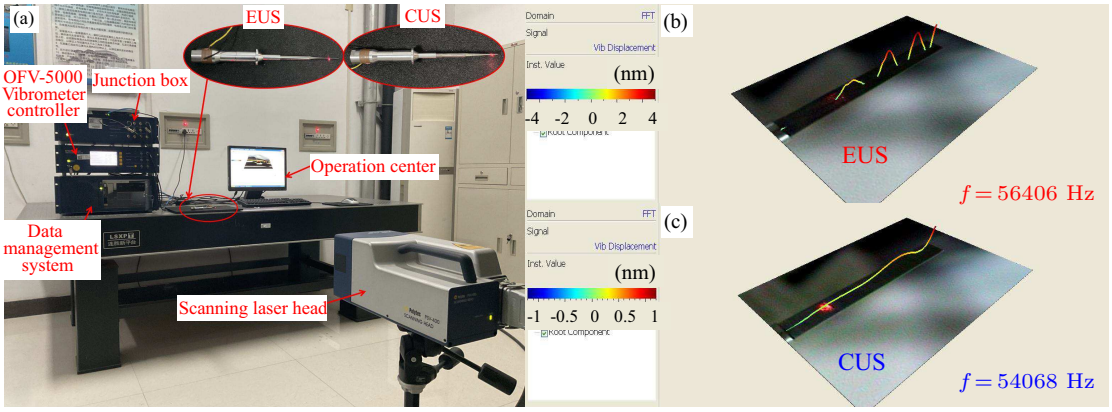


Fig. 10. (a) The vibration testing comparative experiment of two USs by using Polytec scanning vibrator (PSV-400). (b) The displacement distribution on the blade surface of the EUS at a resonance frequency $f_{r-EUS} = 56406$ Hz. (c) The displacement distribution on the blade surface of the CUS at a resonance frequency $f_{r-CUS} = 54068$ Hz.

The comparative experiment was conducted on the vibration performance of the EUS and CUS using a Polytec scanning vibrometer (PSV-400), as shown in Fig. 10(a). The frequency scanning range was set from 50 kHz to 60 kHz. Figure 10(b) shows the displacement distribution on the blade surface of the EUS at a resonance frequency $f_{r-EUS} = 56406$ Hz. Figure 10(c) shows the displacement distribution on the blade surface of the CUS at a resonance frequency $f_{r-CUS} = 54068$ Hz. From the modal observation, more displacement nodes appeared on the surface of the EUS than on the CUS, indicating that adjusting the blade size for modal coupling is a feasible method. In addition, the distance between the EUS displacement nodes became smaller near the cutting head, which means that the bending wave velocity decreased. Therefore, there was more time for the EUS to achieve amplitude accumulation amplification in a short blade. Figure 11 illus-

trates the normalized maximum displacement frequency response curves of two USs. In the resonance state, compared with the CUS, the maximum displacement of the EUS blade has increased by nearly 400%, which is consistent with the results in Section 4 and verifies the feasibility of the EUS in practical operation.

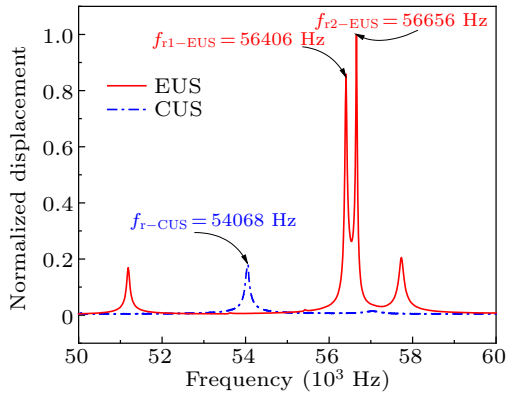


Fig. 11. The normalized maximum displacement frequency response curves of the EUS and the CUS.

6. Conclusions

In summary, we have developed a design scheme for enhancing the ultrasonic scalpel based on vibration mode coupling and symmetrical ABH beam structure. This scheme not only improves the cutting dimension and the vibration amplitude of the EUS compared to the CUS of the same length, but also achieves strong, cumulative amplification of the amplitude on a short blade by embedding the ABH profile, effectively mitigating the performance loss caused by miniaturization. The design method of adjusting the blade size to couple the vibration mode of the EUS has been theoretically and experimentally confirmed, which is expected to be further applied to the design of multimodal ultrasonic vibration systems. Our research can provide a reference for the application of ABHs in the design of ultrasonic vibration devices, and present potential opportunities for developing high-performance ultrasonic medical devices.

Appendix A: Expressions of equivalent mechanical impedances and electrical parameters for EUS components

Expressions of the equivalent mechanical impedances of the back cover plate:

$$Z_1 = \mathrm{j}\rho_1 c_1 \pi R_1^2 \tan(k_1 L_1/2), \tag{A1}$$

$$Z_2 = -\mathrm{j}\rho_1 c_1 \pi R_1^2 / \sin(k_1 L_1), \tag{A2}$$

$$Z_3 = \mathrm{j}\rho_1 c_1 \pi R_2^2 \tan(k_1 L_2/2), \tag{A3}$$

$$Z_4 = -\mathrm{j}\rho_1 c_1 \pi R_2^2 / \sin(k_1 L_2). \tag{A4}$$

Expressions of the equivalent mechanical impedances and electrical parameters of the piezoelectric stack:

$$Z_{p1} = \mathrm{j}\rho_0 c_0 \pi R_2^2 \tan(k_0 P L_0/2), \tag{A5}$$

$$Z_{p2} = -\mathrm{j}\rho_0 c_0 \pi R_2^2 / \sin(k_0 P L_0), \tag{A6}$$

$$n = d_{33}\pi R_2^2/(P L_0 s_{33}^{\mathrm{D}}), \tag{A7}$$

$$C_0 = P\varepsilon_{33}^{\mathrm{T}}(1-k_{33}^2)\pi R_2^2/(P L_0). \tag{A8}$$

Expressions of the equivalent mechanical impedances of the front cover plate:

$$Z_5 = \mathrm{j}\rho_2 c_2 \pi R_2^2 \tan(k_2 L_3/2), \tag{A9}$$

$$Z_6 = -\mathrm{j}\rho_2 c_2 \pi R_2^2 / \sin(k_2 L_3), \tag{A10}$$

$$Z_7 = \frac{-\mathrm{j}\rho_2 c_2 \pi R_2^2 (R_3/R_2 - 1)}{k_2 L_4} - \mathrm{j}\rho_2 c_2 \pi R_2^2 \cot(k_2 L_4) + \frac{\mathrm{j}\rho_2 c_2 \pi R_2^2 (R_3/R_2)}{\sin(k_2 L_4)}, \tag{A11}$$

$$Z_8 = \frac{-\mathrm{j}\rho_2 c_2 \pi R_3^2 (R_2/R_3 - 1)}{k_2 L_4} - \mathrm{j}\rho_2 c_2 \pi R_3^2 \cot(k_2 L_4) + \frac{\mathrm{j}\rho_2 c_2 \pi R_4^2 (R_3/R_2)}{\sin(k_2 L_4)}, \tag{A12}$$

$$Z_9 = -\frac{\mathrm{j}\rho_2 c_2 \pi R_4^2 (R_3/R_2)}{\sin(k_2 L_4)}, \tag{A13}$$

$$Z_{10} = \mathrm{j}\rho_2 c_2 \pi R_3^2 \tan(k_2 L_5/2), \tag{A14}$$

$$Z_{11} = -\mathrm{j}\rho_2 c_2 \pi R_3^2 / \sin(k_2 L_5). \tag{A15}$$

Expressions of the equivalent mechanical impedances of the concentrator:

$$Z_{12} = \mathrm{j}\rho_2 c_2 \pi R_4^2 \tan(k_2 L_6/2), \tag{A16}$$

$$Z_{13} = -\mathrm{j}\rho_2 c_2 \pi R_4^2 / \sin(k_2 L_6), \tag{A17}$$

$$Z_{14} = \mathrm{j}\rho_2 c_2 \pi R_5^2 \tan(k_2 L_7/2), \tag{A18}$$

$$Z_{15} = -\mathrm{j}\rho_2 c_2 \pi R_5^2 / \sin(k_2 L_7), \tag{A19}$$

$$Z_{16} = \frac{-\mathrm{j}\rho_2 c_2 \pi R_5^2 (R_7/R_5 - 1)}{k_2 L_8} - \mathrm{j}\rho_2 c_2 \pi R_5^2 \cot(k_2 L_8) + \frac{\mathrm{j}\rho_2 c_2 \pi R_5^2 \left(\frac{R_7}{R_5}\right)}{\sin(k_2 L_8)}, \tag{A20}$$

$$Z_{17} = \frac{-\mathrm{j}\rho_2 c_2 \pi R_7^2 (R_5/R_7 - 1)}{k_2 L_8} - \mathrm{j}\rho_2 c_2 \pi R_7^2 \cot(k_2 L_8) + \frac{\mathrm{j}\rho_2 c_2 \pi R_5^2 \left(\frac{R_7}{R_5}\right)}{\sin(k_2 L_8)}, \tag{A21}$$

$$Z_{18} = -\frac{\mathrm{j}\rho_2 c_2 \pi R_5^2 \left(\frac{R_7}{R_5}\right)}{\sin(k_2 L_8)}, \tag{A22}$$

$$Z_{19-1} = \mathrm{j}\rho_2 c_2 \pi R_7^2 \tan\left[k_2\left(L_9 - \frac{L_{11}}{2}\right)/2\right], \tag{A23}$$

$$Z_{20-1} = -\mathrm{j}\rho_2 c_2 \pi R_7^2 / \sin\left[k_2\left(L_9 - \frac{L_{11}}{2}\right)\right], \tag{A24}$$

$$Z_{19-2} = \mathrm{j}\rho_2 c_2 \pi (R_7^2 - R_9^2) \tan(k_2 L_{11}/4), \tag{A25}$$

$$Z_{20-2} = -\mathrm{j}\rho_2 c_2 \pi (R_7^2 - R_9^2) / \sin(k_2 L_{11}/2). \tag{A26}$$

Expressions of the equivalent mechanical impedances of the bolt:

$$Z_{01-1} = \mathrm{j}\rho_1 c_1 \pi R_9^2 \tan(k_1 L_{11}/4), \tag{A27}$$

$$Z_{02-1} = -\mathrm{j}\rho_1 c_1 \pi R_9^2 / \sin(k_1 L_{11}/2), \tag{A28}$$

$$Z_{01-2} = \mathrm{j}\rho_1 c_1 \pi R_9^2 \tan(k_1 L_{11}/4), \tag{A29}$$

$$Z_{02-2} = -\mathrm{j}\rho_1 c_1 \pi R_9^2 / \sin(k_1 L_{11}/2). \tag{A30}$$

Expressions of the equivalent mechanical impedances of the ABH blade:

$$Z_{21-1} = \mathrm{j}\rho_3 c_3 \pi (R_7^2 - R_9^2) \tan(k_3 L_{11}/4), \tag{A31}$$

$$Z_{22-1} = -\mathrm{j}\rho_3 c_3 \pi (R_7^2 - R_9^2) / \sin(k_3 L_{11}/2), \tag{A32}$$

$$Z_{21-2} = \mathrm{j}\rho_3 c_3 \pi R_7^2 \tan\left[k_3 \left(L_{10} - \frac{L_{11}}{2}\right)/2\right], \tag{A33}$$

$$Z_{22-2} = -\mathrm{j}\rho_3 c_3 \pi R_7^2 / \sin\left[k_3 \left(L_{10} - \frac{L_{11}}{2}\right)\right], \tag{A34}$$

$$Z_{23} = -(A_{11} + 1)/A_{12}, \tag{A35}$$

$$Z_{24} = (A_{22} - 1)/A_{12}, \tag{A36}$$

$$Z_{25} = 1/A_{12}, \tag{A37}$$

$$U = (A_{12}A_{21} - A_{11}A_{22} - 1)v_{\mathrm{L2}}/A_{12}. \tag{A38}$$

Acknowledgements

Project supported by the Key Program of the National Natural Science Foundation of China (Grant No. 12534018) and the General Programs of the National Natural Science Foundation of China (Grant Nos. 12174240 and 12574498).

References

[1] Luciani N, Anselmi A, Gaudino M, Nasso G, Glieca F, Martinelli L, Santarelli F, Perisano M and Possati G 2005 *The Annals of Thoracic Surgery* **80** 934
[2] Bozkurt G, Turri-Zanoni M, Russo F, Elhassan H A, Castelnuovo P and Battaglia P 2019 *World Neurosurgery* **123** 23
[3] Wang S, Shan J J and Lin S Y 2024 *Chin. Phys. B* **33** 104302
[4] Zhang S B, Chen Z R, Wu H Q, Li G Z and Wu Y B 2023 *Ultrasonics* **131** 106966
[5] Schafer M E 2023 *IEEE Trans. Ultrason. Ferroelectr. Freq. Control* **70** 147
[6] Cleary R, Li X and Lucas M 2021 *J. Acoust. Soc. Am.* **150** 2163
[7] Li Z Y, Li J A, Wu Z H, Chen Y H, Yeerbulati M and Xu Q S 2024 *IEEE Trans. Rob.* **40** 2306
[8] Li X, Stritch T, Manley K and Lucas M 2021 *IEEE Trans. Ultrason. Ferroelectr. Freq. Control* **68** 2543
[9] Chen Q, Yao M, Lin L, Liu X N, Liu Y Q, Wang F F, Tang Y X, Zhang Q Z, Lin D, Luo H S and Zhao X Y 2025 *Sens. Actuator A Phys.* **382** 116149
[10] Cleary R, Wallace R, Simpson H, Kontorinis G and Lucas M 2022 *Ultrasonics* **124** 106756
[11] Li J H, Dong X Y, Zhang G H, Guo Z C, Zhang G K and Shi C Y 2021 *IEEE Access* **9** 10951
[12] Zhang S B, Guo Y F, Chen Z C, Li G Z, Guo Q Y, Wu Y B and Zeng J 2021 *Ultrasonics* **109** 106259
[13] Le Bourlout Y, Ehnholm G and Nieminen H J 2023 *J. Acoust. Soc. Am.* **154** 3388
[14] Yao G, Wu F, Lucas M, Zheng L J, Wang C Y and Gu H 2023 *Ultrasonics* **135** 107113
[15] Krylov V V 2014 *IEEE Trans. Ultrason. Ferroelectr. Freq. Control* **61** 1296
[16] Pelat A, Gautier F, Conlon S C and Semperlotti F 2020 *J. Sound Vib.* **476** 115316
[17] Mi Y Z, Zhai W, Cheng L, Xi C Y and Yu X 2021 *Appl. Phys. Lett.* **118** 114101
[18] Bravo T and Maury C 2023 *J. Sound Vib.* **561** 117825
[19] Zhang Z H, Geng M J, Zhao C Y, Cao Y J and Wang P 2025 *Appl. Acoust.* **231** 110546
[20] Chang L and Cheng L 2025 *J. Sound Vib.* **608** 119082
[21] Zhu H, Li J B, Ge X H and Li D P 2025 *Acta Phys. Sin.* **74** 194301 (in Chinese)
[22] Liu Y, Chen C and Lin S Y 2025 *Ultrasonics* **151** 107630
[23] Lee J Y and Jeon W 2017 *J. Acoust. Soc. Am.* **141** 1437
[24] Deng J, Gao N S, Chen X, Han B and Ji H L 2023 *Mech. Syst. Signal Process.* **191** 110182
[25] Deng J and Gao N S 2022 *Int. J. Mech. Sci.* **233** 107641
[26] Zhang L F, Tang X, Qin Z Y and Chu F L 2022 *Appl. Phys. Lett.* **121** 013902
[27] Mousavi A, Berggren M, Hägg L and Wadbro E 2024 *J. Acoust. Soc. Am.* **155** 742
[28] Liu P Z, Huang H Y, Wang X, Tang Q, Qi X M, Su S F, Xiang Z H and Hu J H 2023 *Mech. Syst. Signal Process.* **188** 109991
[29] Liu P Z, Tian Z H, Yang K C, Naquin T D, Hao N J, Huang H Y, Chen J Y, Ma Q X, Bachman H, Zhang P, Xu X H, Hu J H, Huang T J 2022 *Sci. Adv.* **8** eabm2592
[30] Wang Y, Chen C, Ren W B, Chen H Q and Lin S Y 2025 *Sens. Actuator A Phys.* **395** 117042
[31] Chen C, Tang Y F, Ren W B, Wang Y, Guo J Z and Lin S Y 2025 *Ultrasonics* **143** 107417
[32] Chen C, Liu Y, Wang C H, Guo J Z and Lin S Y 2025 *Ultrason. Sonochem.* **111** 107106
[33] Wang L, Hofmann V, Bai F S, Jin J M and Twiefel J 2018 *Mech. Syst. Signal Process.* **108** 216
[34] Dong Y L, Chen C and Lin S Y 2023 *Acta Phys. Sin.* **72** 054304 (in Chinese)
[35] Chen C, Dong Y L, Wang S, Hu L Q and Lin S Y 2022 *J. Acoust. Soc. Am.* **151** 2712
[36] Zhou G P and Li M X 2000 *J. Acoust. Soc. Am.* **107** 1358